Chinese Chemical Letters 36 (2025) 110211

Contents lists available at ScienceDirect

Chinese Chemical Letters

journal homepage: www.elsevier.com/locate/cclet

NIR driven catalytic enhanced acute lung injury therapy by using polydopamine@Co nanozyme *via* scavenging ROS

Xiaoshuai Wu[a,1], Bailei Wang[b,1], Yichen Li[c,1], Xiaoxuan Guan[c], Mingjing Yin[d], Wenquan Lv[d], Yin Chen[a], Fei Lu[d], Tao Qin[d], Huyang Gao[c], Weiqian Jin[c], Yifu Huang[b], Cuiping Li[e,f,*], Ming Gao[c,*], Junyu Lu[a,*]

[a] *Intensive Care Unit, The Second Affiliated Hospital of Guangxi Medical University, Nanning 530007, China*
[b] *Department of Critical Care Medicine, The Ninth Affiliated Hospital of Guangxi Medical University, Beihai 536000, China*
[c] *Life Sciences Institute, Guangxi Medical University, Nanning 530021, China*
[d] *Department of Emergency, The First Affiliated Hospital of Guangxi Medical University, Nanning 530021, China*
[e] *College & Hospital of Stomatology, Guangxi Medical University, Nanning 530021, China*
[f] *Guangxi Key Laboratory of Oral and Maxillofacial Rehabilitation and Reconstruction, Guangxi Medical University, Nanning 530021, China*

ARTICLE INFO

Article history:
Received 12 April 2024
Revised 26 June 2024
Accepted 3 July 2024
Available online 4 July 2024

Keywords:
Acute lung injury
NIR driven
Nanozyme
ROS scavenging
M2 directional polarization

ABSTRACT

Acute lung injury (ALI) was characterized by excessive reactive oxygen species (ROS) levels and inflammatory response in the lung. Scavenging ROS could inhibit the excessive inflammatory response, further treating ALI. Herein, we designed a novel nanozyme (P@Co) comprised of polydopamine (PDA) nanoparticles (NPs) loading with ultra-small Co, combining with near infrared (NIR) irradiation, which could efficiently scavenge intracellular ROS and suppress inflammatory responses against ALI. For lipopolysaccharide (LPS) induced macrophages, P@Co + NIR presented excellent antioxidant and anti-inflammatory capacities through lowering intracellular ROS levels, decreasing the expression levels of interleukin-6 (IL-6) and tumor necrosis factor-α (TNF-α) as well as inducing macrophage M2 directional polarization. Significantly, it displayed the outstanding activities of lowering acute lung inflammation, relieving diffuse alveolar damage, and up-regulating heat shock protein 70 (HSP70) expression, resulting in synergistic enhanced ALI therapy effect. It offers a novel strategy for the clinical treatment of ROS related diseases.

Acute lung injury (ALI) encompasses the significant impairment of alveolar epithelial cells and capillary endothelial cells, arising from direct and indirect insults to lung tissue, including infections, severe trauma, and sepsis [1]. When reaching a more serious condition, it becomes acute respiratory distress syndrome (ARDS) with the mortality ratio of 25%–40% [2]. Even if the patients can be rescued, it significantly affects the life quality of survivors [3]. Ample evidences demonstrate that excessive inflammatory responses cause the cytokine storm in the lung, ultimately leading to ALI [4]. And it has confirmed that reactive oxygen species (ROS) including hydroxyl radical ($^{\bullet}OH$), superoxide anion ($^{\bullet}O_2^-$) and singlet oxygen ($^1O_2$) significantly contribute to the generation of overwhelming inflammation in lung cells [5]. Therefore, eliminating ROS can inhibit the excessive inflammatory responses in the organ, the key to ALI therapy [6].

As a serial of nanomaterials with catalytic activities such as superoxide dismutase (SOD), catalase (CAT), and glutathione peroxidase (GPx), nanozymes possess the advantages of high bioavailability, good dispersibility, and minimal toxic side effects [7,8]. They can produce or clear ROS to regulate oxidative stress, thus achieving remarkable researches in the treatment of diseases such as tumors [9-12], Parkinson's disease [13], and pneumonia [14]. Hu and his team developed a multienzyme-mimicking redox nanozyme (PtMnIr) capable of efficient ROS generation and cellular homeostasis disruption, yielding a powerful and synergistic combination of enzymatic and electrodynamic therapies targeting malignant tumors [15]. Yang *et al.* also developed an Fe-curcumin nanozyme that possessed the capability of directing intracellular ROS scavenging and exhibiting anti-inflammation effectiveness for treating ALI [6]. Although nanozymes with excellent catalytic activities could achieve the treatment of ROS derived diseases, their clini-

* Corresponding authors.
E-mail addresses: gxcuiping@sina.com (C. Li), gaoming1983125@hotmail.com (M. Gao), junyulu@gxmu.edu.cn (J. Lu).
[1] These authors contributed equally to this work.

https://doi.org/10.1016/j.cclet.2024.110211
1001-8417/

cal application was limited by high cost with low yield rate, and instability not suitable for various environments. Therefore, it remains a challenge of designing a nanozyme with controllable ROS scavenging ability to achieve synergistic enhancement in diseases therapy.

Polydopamine (PDA) was synthesized *via* self-polymerization of dopamine (DA) under weak alkaline conditions with magnetic stirring [16-18]. As relative stable nanoparticles (NPs), they displayed excellent biocompatibility and biodegradability, photothermal conversion ability, and high loading of components [19]. Furthermore, PDA based NPs presented multiple ROS scavenging capacities due to their large amount of catechol and imine groups, further applied in alleviating ROS derived diseases [20]. Significantly, after hybridizing with metal elements such as Pd [21] or Cu [22], the metal elements could be stable and firmly dispersed on the surface of PDA, leading to the improvement of the dispersion of metal elements, and also enhanced ROS scavenging ability. Thus, these PDA derivatives could finally achieve high efficacy of diseases therapy [23,24]. In the meantime, as a trace element, a certain amount of Co can maintain the normal metabolic and physiological functions of cells, helpful for normal human functions. Considering the conversion of Co^{2+}/Co^{3+}, a amount of evidences demonstrated that Co possessed outstanding catalytic activity, widely applied in biomedical fields [25,26]. Chen *et al.* developed a Co coordinated on N-doped porous carbon (Co-SAs@NC), which displayed CAT and SOD like activities for tumor therapy [27]. And Qu *et al.* designed a single atom catalyst (Co/PMCS) with unsaturated active Co-porphyrin centers, which rapidly eliminated ROS by imitating SOD, CAT and GPx for sepsis therapy [26].

Inspired by the above, we designed a novel nanozyme (P@Co) by loading ultra-small Co on the surface of PDA. Compared with PDA alone, it displayed enhanced ROS scavenging and photothermal capacities for P@Co, leading to the synergistic enhancement of ALI therapy. For lipopolysaccharide (LPS) induced macrophages, it obviously lowered the expression levels of inflammatory factors, and induced M2 directional polarization of macrophages for P@Co combining with near infrared (NIR) irradiation. And it also significantly alleviated the symptoms of ALI rats for P@Co + NIR. In conclusion, it offered a promising strategy for ALI therapy *via* ROS scavenging and could be also promoted for the treatment of other ROS derived diseases.

Herein, PDA was first fabricated through the redox polymerization of DA after dissolving DA in the mixture of deionized water (DI) water and ethanol, followed by adjusting pH 9.0. And P@Co was prepared by *in situ* reduction of $Co(OAc)_2$ to form ultra-small Co on the surface of PDA (Fig. 1A). As displayed in Fig. S1 (Supporting information), DA was in white color and it became black for PDA. After loading with $Co(OAc)_2$ (brown), it was still black for P@Co. From ultraviolet–visible spectroscopy (UV–vis) results, obvious absorbance peak was observed at 280 nm for DA, attributed by the double bonds of benzene. However, it disappeared after forming PDA. And there were no absorbance peaks for $Co(OAc)_2$ and P@Co as well (Fig. S2 in Supporting information). Similarly, the zeta potential was 14.1 ± 1.5 mV for DA, and it was -24.7 ± 1.2, 29.4 ± 0.1 and -44.5 ± 0.4 mV for PDA, $Co(OAc)_2$ and P@Co, respectively (Fig. S3 and Table S1 in Supporting information). As illustrated in Fig. S4 (Supporting information), the obvious broad peak appeared around 3700–3100 cm^{-1} for PDA while there were no changes for P@Co after Co loading. In the meantime, there were no changes in crystallization structure between PDA and P@Co, only with a single peak existed at 21.6° (Fig. S5 in Supporting information). It also presented similar peaks in Raman spectroscopy, indicating the same molecular structure for PDA and P@Co (Fig. S6 in Supporting information). From transmission electron microscopy (TEM)-mapping results, PDA was in spherical shape and its diameter size was 59.9 ± 9.4 nm, only with C, N and O elements observed in Fig. S7 (Supporting information). Nevertheless, it maintained its spherical shape for P@Co after Co loading, with C, N, O and Co elements observed (Fig. 1B). Furthermore, the element composition of PDA and P@Co was also characterized by X-ray photoelectron spectroscopy (XPS). As shown in Fig. S8 (Supporting information), it exhibited C, N and O elements both for PDA and P@Co, whereas Co element was exclusively detected for P@Co, also proving the successful Co loading. Finally, during the temperature range from 20 °C to 800 °C, the weight loss ratio was 65.631% and 62.584% for PDA and P@Co respectively (Fig. S9 in Supporting information). After calculation, Co loading ratio was 3.1% ± 0.1%. And the comprehensive element composition was illustrated in Table S2 (Supporting information). After Co loading, it did not alter the color, molecular structure, crystallization, and morphology of P@Co. However, it changed the zeta potential and element composition between PDA and P@Co.

For *in vivo* clinical application, it is required that NPs possess a certain level of dispersion. The dispersion ability testing was implemented by dispersing NPs in different solutions. As exhibited in Fig. S10 (Supporting information), PDA and P@Co were well dispersed in various solutions at the beginning. At 12 h, it was almost totally settled on the bottom of phosphate buffered saline (PBS), Dulbecco's modified eagle's medium (DMEM) and 5 mmol/L H_2O_2, respectively for PDA. However, P@Co was totally on the bottom of PBS, DMEM and 5 mmol/L H_2O_2 after 24 h. Significantly, P@Co was well dispersed in fetal bovine serum (FBS) for 24 h. Thus, the dispersion ability of P@Co was better than that of PDA due to Co loading, which enhanced the number of surface charges of P@Co and improved its stability [22].

Photothermal effect was investigated by monitoring the temperature changes under NIR irradiation by thermal camera (Fig. 1C). As shown in i of Fig. 1D, temperature increased *versus* irradiation time for PDA and P@Co with the same concentration of 100 μg/mL while no temperatures changed for PBS. It presented similar tendency for PDA and P@Co, increased to 62.7 and 60.8 °C, respectively under NIR irradiation for 15 min. After Co loading, it slightly diminished the photothermal effects of P@Co, still close to PDA. Generally, their photothermal effects mainly originated from PDA itself [28]. Compared to PDA, Co loading could block the absorption of NIR, and further reduced its photothermal effect [29]. And if increasing the concentration of P@Co, it also increased its photothermal effect, where it was 25.8, 51.3, 60.7 and 66.6 °C for 0, 50, 100 and 200 μg/mL of P@Co after 15 min' irradiation (ii of Fig. 1D). Meanwhile, the temperature increased with the increase of irradiation intensity (iii of Fig. 1D). Significantly, the temperature change maintained almost the same trend during 4 "on" and "off" cycles (iv of Fig. 1D), indicating the excellent photothermal stability. In conclusion, it exhibited remarkable photothermal efficiency and stability for P@Co, enhanced by increasing PDA concentrations and power intensities.

ROS scavenging capacity was qualified tested by electron spin resonance (ESR). As exhibited in i of Fig. 1E, compared to control group, PDA could decrease the intensity of $^{\bullet}OH$, and P@Co more effectively lowered the intensity of $^{\bullet}OH$. Specifically, the intensity of $^{\bullet}OH$ significantly decreased for P@Co + NIR. It presented the same tendency for $^{\bullet}O_2^-$ (ii of Fig. 1E) and $^1O_2$ (iii of Fig. 1E) scavenging, with the order of scavenging ratio: P@Co + NIR > P@Co > PDA. In the meantime, ROS testing kits were applied to investigate the ROS scavenging capacity of NPs. As exhibited in i of Fig. 1F, it obviously presented $^{\bullet}OH$ scavenging capacity, where it was 32.9% ± 0.1%, 39.5% ± 1.4% and 41.7% ± 0.5% for PDA, P@Co and P@Co + NIR with the same concentration of 100 μg/mL (Table S4 in Supporting information). If the concentration of P@Co increased from 50 μg/mL to 200 μg/mL, the corresponding scavenging ratio jumped from 37.2% ± 0.8% to 42.4% ± 0.4% (Fig. S11 and Table S5 in Supporting information). The similar tendency was observed for

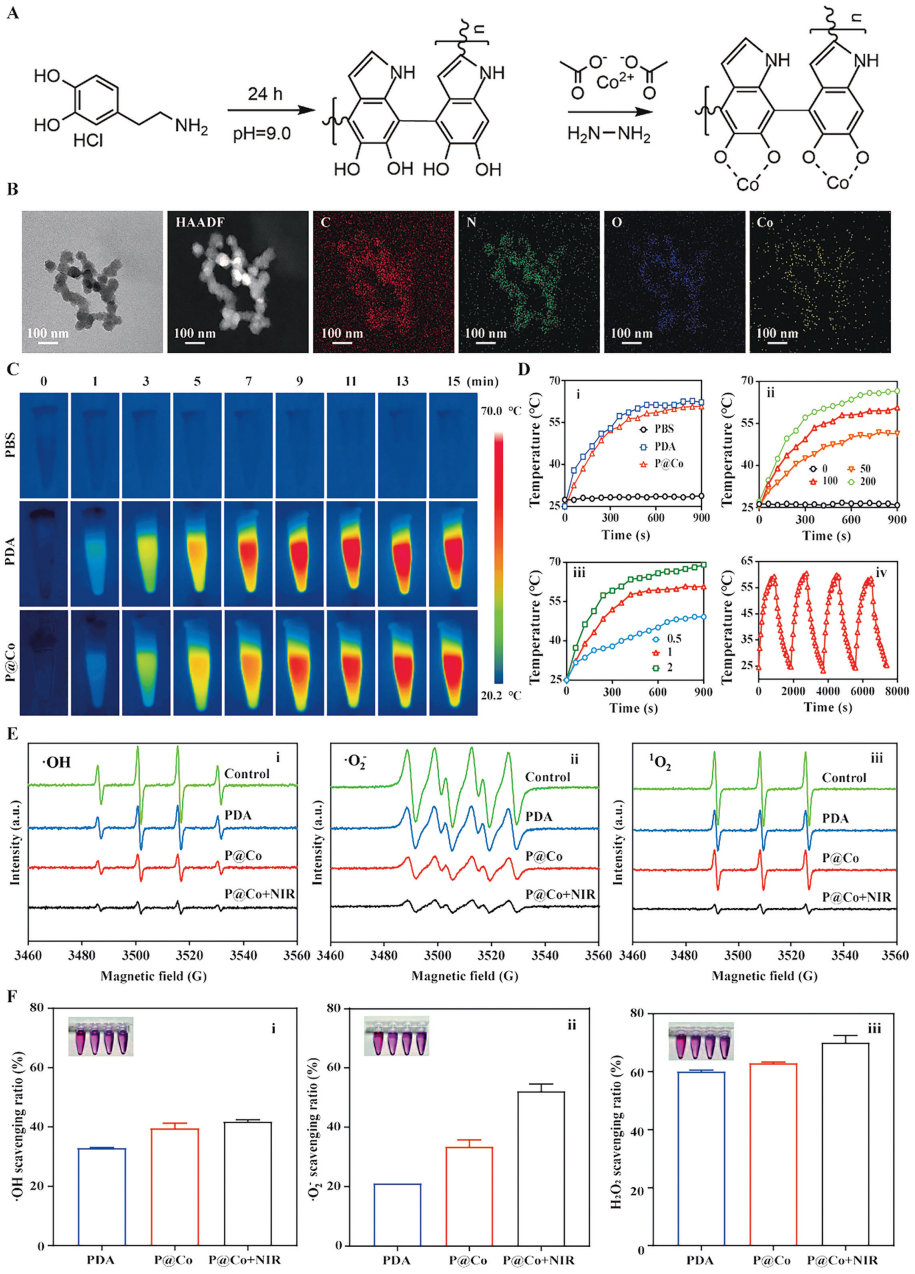

Fig. 1. Preparation and physicochemical characterization of P@Co. (A) Synthesis procedure of P@Co. (B) TEM-mapping results of P@Co. Scale bar: 100 nm. (C) Photothermal images of different nanozymes (PDA and P@Co) with the same concentration of 100 μg/mL under NIR irradiation (1 W/cm^2) *versus* time. (D) Temperature changes of PBS, PDA and P@Co with the same concentration of 100 μg/mL under NIR irradiation (1 W/cm^2) (i), different concentrations (0, 50, 100 and 200 μg/mL) of P@Co under NIR irradiation (1 W/cm^2) (ii), 100 μg/mL P@Co under different power intensities of NIR irradiation (0.5, 1 and 2 W/cm^2) (iii) *versus* time, and photothermal stability of 100 μg/mL P@Co under NIR irradiation (1 W/cm^2) for 4 "on" and "off" cycles (iv). (E) ESR results of ROS scavenging ability of different nanozymes: $^{\bullet}OH$ (i), $^{\bullet}O_2^-$ (ii) and $^1O_2$ (iii). (F) ROS scavenging capacity of different nanozymes by ROS testing kits: $^{\bullet}OH$ (i), $^{\bullet}O_2^-$ (ii) and H_2O_2 (iii). Data are presented as mean ± standard deviation (SD) ($n \geq 3$).

$^{\bullet}O_2^-$ (ii of Fig. 1F) and $^1O_2$ (iii of Fig. 1F) scavenging, which was in the order of P@Co + NIR > P@Co > PDA with the same concentration. And the enhanced scavenging ratio was obtained by increasing the concentration of P@Co (Figs. S12 and S13 in Supporting information). For PDA itself, it possessed a certain of ROS scavenging ability, due to its huge amount of reducing groups. The enhanced ROS scavenging capacity was achieved for P@Co after Co loading. Most significantly, NIR irradiation speed up the movement of Co, further most efficiently leading to improved ROS scavenging ability [30,31].

Cell viability was evaluated by using cell counting kit-8 (CCK-8) assay. As revealed in Fig. S14 (Supporting information), the cell viability was above 92.5% for P@Co with the concentration ranges from 0 to 75 μg/mL. When the concentration was ascended to 150 μg/mL, cell viability significantly decreased. Thus, 100 μg/mL NPs was considered to implement the further experiment. LPS stimulation was commonly applied to induce *in vitro* and *in vivo* ALI models, due to the fact that this model is similar to the pathological characteristics of ALI in humans [32,33]. The protection ability of NPs for LPS induced cells was also investigated by live/dead staining. As shown in Fig. S15 (Supporting information), in normal group, a huge amount of live cells were observed, whereas dead cells was negligible, with the live/dead ratio of 95.2% (Fig. S16 in Supporting information). However, after LPS induction, a lot of dead cells was observed and a few of live cells existed in control group. The corresponding live/dead ratio decreased to 4.5%. Com-

pared to PDA, P@Co significantly increased the number of live cells, resulting in a live/dead ratio of 83.9%. Notably, the live/dead ratio further increased to 93.2% when P@Co was combined with NIR irradiation. Thus, P@Co + NIR with enhanced ROS scavenging ability was always more helpful to protect the cells avoiding the damage from oxidative stress.

To fully utilize its functions, it anticipated that P@Co could be uptake by macrophages. As indicated in Fig. S17 (Supporting information), it displayed that no fluorescence was observed for cells at the beginning. After 3 h incubation, a little of fluorescent intensity was observed inside cells. The significant enhanced fluorescence was observed for cells at 6 h, indicating the obvious cellular uptake of P@Co (Fig. S18 in Supporting information).

The intracellular ROS levels were measured to assess the antioxidant capacity of NPs. As depicted in Fig. 2A, the minimal red fluorescence was observed in normal group (dihydroethidium (DHE) probe), whereas a substantial amount of red fluorescence was found in control group. PDA could decrease a certain of fluorescent intensity, indicating its intracellular ROS scavenging ability. However, it exhibited that P@Co possessed more efficient ROS scavenging ability, significantly enhanced for P@Co + NIR. It was the same trend for dichlorodihy drofluorescein (DCF) probe, the mean fluorescent intensity (MFI) was significantly ascended for control group after LPS induction, which significantly decreased for PDA, P@Co and P@Co + NIR respectively (Fig. 2B).

Subsequently, immunohistochemical staining was employed to evaluate the anti-inflammatory properties of NPs. As indicated in Fig. 2C, it displayed that the expression levels of interleukin-10 (IL-10) and tumor necrosis factor-α (TNF-α) were in the relative low levels for normal cells, which significantly increased after LPS induction, indicated by the enhanced staining intensity. Specifically, NPs could up-regulate the expression level of IL-10 and down-regulate the expression level of TNF-α, with the order of P@Co + NIR > P@Co > PDA (Fig. 2D).

Furthermore, enzyme-linked immunosorbent assay (ELISA) was employed to assess the expression levels of inflammatory factors in the supernatant of treated cells. As illustrated in i of Fig. 2E, compared to normal cells with 21.7 ± 0.7 pg/mL, it was 42.6 ± 3.0 pg/mL for control group after LPS induction. PDA and P@Co could lower IL-6 expression level to 32.1 ± 2.9 and 31.9 ± 1.1 pg/mL, respectively. In particular, P@Co + NIR presented the most efficient down-regulation effect of IL-6 expression level (23.2 ± 1.6 pg/mL). Meanwhile, for TNF-α expression level, it displayed the same order: control group > PDA > P@Co > P@Co + NIR > normal group (ii of Fig. 2E).

Finally, quantitative real-time polymerase chain reaction (qRT-PCR) technique was applied to analyze the relative expression levels of genes. As illustrated in Fig. 2F, compared to normal cells, the inflammatory genes (IL-6, iIL-1β, inducible nitric oxide synthase (iNOS) and TNF-α) were significantly ascended for control group after LPS induction. PDA and P@Co could significantly lower the expression levels of IL-6, IL-1β, iNOS and TNF-α, where it exhibited the most efficient down-regulation of these genes for P@Co + NIR. However, for anti-inflammatory genes (IL-10 and TNF-α), it was in high levels for normal cells. After LPS induction, the corresponding anti-inflammatory genes significantly decreased to 1.4 ± 0.8 and 1.1 ± 0.4, respectively. And NPs could improve the expression levels of IL-10 and TNF-α. Among them, P@Co + NIR most obviously improved the anti-inflammatory genes expression to 10.9 ± 2.2 and 6.6 ± 0.7, respectively. Besides, it also confirmed that P@Co + NIR significantly down-regulated M1 type genes, and up-regulated M2 type genes, indicating the most efficient induction of M2 directional polarization. Most importantly, compared to P@Co alone, it also displayed the high expression of heat shock protein 70 (HSP70) gene for P@Co + NIR (Fig. S19 in Supporting information).

For *in vivo* animal experiment, male Sprague-Dawley rats (150–200 g) were obtained from Experimental Animal Center of Guangxi Medical University. All experiments were conducted according to institutional guidelines and approved by Animal Ethics Committee of Guangxi Medical University. As revealed in Fig. S20 (Supporting information), there was no detectable fluorescent intensity observed in any organs of sham group or P@Co. Specifically, for Cy5, the obvious decrease of fluorescence was displayed in the lung *versus* time while no signal was found in other organs. However, for Cy5-P@Co, obvious fluorescence appeared in the lung and a little fluorescence existed in the kidney. Furthermore, it demonstrated that P@Co could stay in the lung for a certain of time and gradually be cleared after 12 h. After statistical analysis, the obvious decrease of fluorescence was observed in the lung for Cy5-P@Co *versus* time while it could maintain around 12 h (Fig. S21 in Supporting information). In addition, blood biocompatibility was assessed by hemolysis test. As illustrated in Fig. S22 (Supporting information), it displayed the excellent blood biocompatibility for PDA and P@Co during the concentration range from 0 to 200 μg/mL, without any hemolysis phenomenon observed. After calculation, the hemolysis ratio was around 0.30%–0.80%, all below 5%.

To assess the feasibility of *in vivo* photothermal therapy, rats were instillation (IT) injected with P@Co, and monitored the temperature changes under NIR irradiation by thermal camera. Compared to sham group, obvious temperature increased *versus* time for P@Co after IT injection for 1 h (Fig. S23 in Supporting information). By statistical analysis, the temperature increased from 35.2 °C to 49.2 °C for P@Co during irradiation while it maintained almost the same temperatures for sham group (Fig. S24 in Supporting information).

To avoid damaging other organs, we chose IT injection of LPS to establish ALI model for further evaluation [6,32,33]. *In vivo* therapy effect was initially evaluated by testing the blood indicators. As listed in Fig. S25 and Table S6 (Supporting information), there were no differences in red blood cell (RBC), alanine aminotransferase (ALT), activated partial thromboplastin time (APTT), and prothrombin Time (PT) for all groups. LPS induction could up-regulate white blood cell (WBC), aspartate aminotransferase (AST), and creatinine (CREA), and down-regulate platelet count (PLT) and creatinine clearance rate (Ccr) compared to sham group. And P@Co could slightly lower the levels of WBC and AST, and increase the levels of PLT and Ccr, enhanced for P@Co + NIR. Although the significant difference was not high for blood indicators statistically, slight tendency still existed for some indicators like WBC, PLT, AST, Ccr and CREA. Similarly, the wet/dry ratio was 4.78 ± 0.1, 5.03 ± 0.1, 4.89 ± 0.1 and 4.84 ± 0.1 for sham group, ALI group, P@Co and P@Co + NIR respectively (Fig. 3A).

Next, the macroscopic view of lungs of all groups were observed. As shown in Fig. 3B, the lung was pink with smooth surface for sham group while it became dark red with obvious congestive sites observed for ALI group. However, congestive sites were apparently relieved for P@Co. Especially for P@Co + NIR, the lungs almost returned to normal state, close to sham group. The inflammatory factors expression levels of blood serum and lung tissue were analyzed by ELISA. As revealed in i of Fig. 3C, the IL-6 expression of serum was in high levels for ALI group, compared to sham group. P@Co could lower IL-6 expression level, which was also descended for P@Co + NIR. And the same tendency was observed for TNF-α expression level of serum, with the order of ALI group > P@Co > P@Co + NIR > sham group (ii of Fig. 3C). Similarly, for the homogenate of lung tissue, IL-6 and TNF-α expression levels were ascended for ALI group compared to sham group. P@Co with or without NIR irradiation could lower the corresponding expression levels. And the order of IL-6 and TNF-α expression levels were: ALI group > P@Co > P@Co + NIR > sham group (Fig. 3D). And the lung tissue was evaluated by hematoxylin-eosin

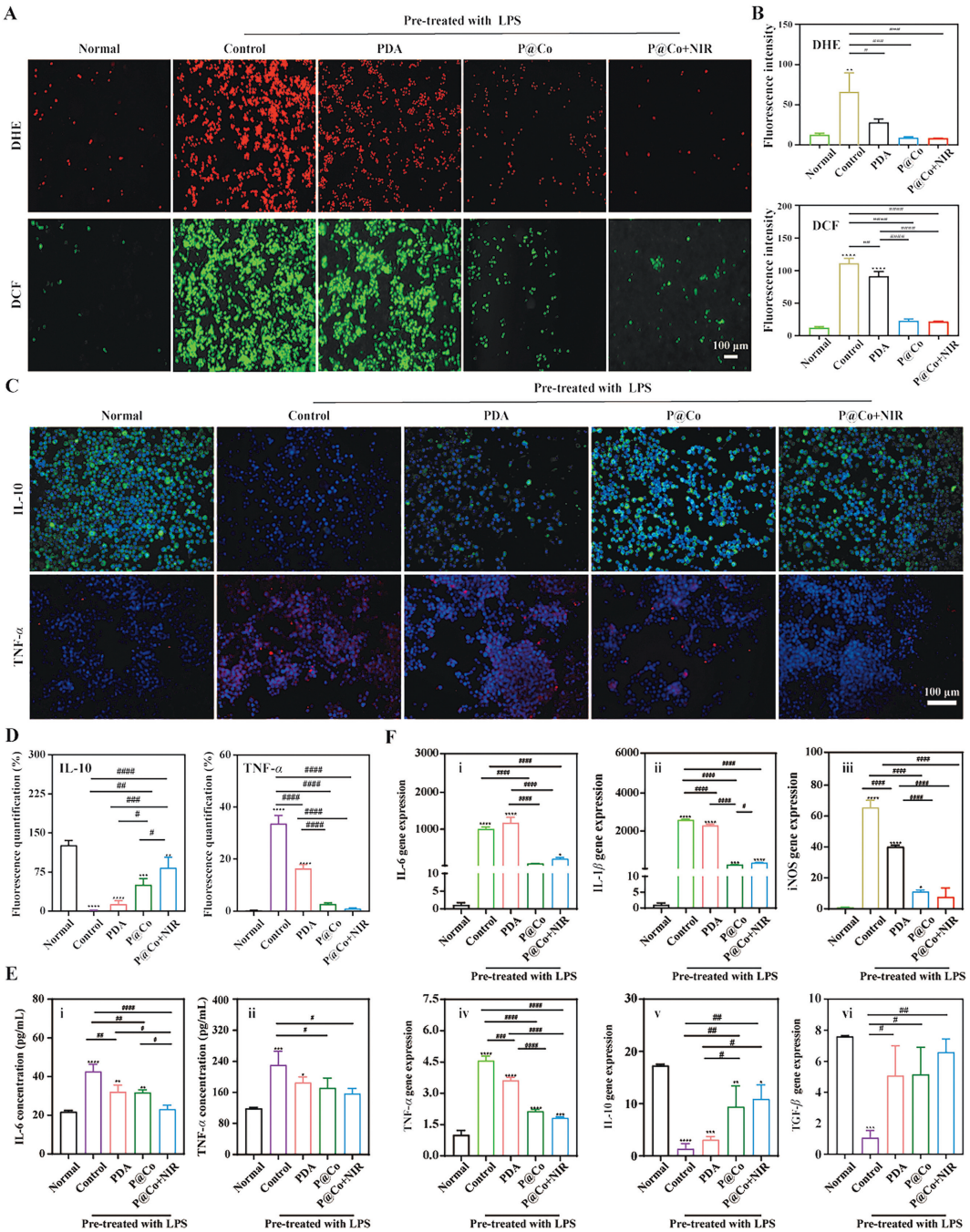

Fig. 2. Antioxidant and anti-inflammation capacity in cellular levels. (A) Intracellular ROS (DHE and DCF) levels of treated cells by fluorescent microscope and the corresponding quantified results (B). (C) Inflammatory factors expression levels of treated cells by fluorescent microscope and the corresponding quantified results (D). (E) Inflammatory factors expression levels of the supernatent of treated cells by ELISA. (F) Genes (IL-6 (i), IL-1β (ii), iNOS (iii), TNF-α (iv), IL-10 (v) and transforming growth factor-β (TGF-β) (vi)) expression levels of treated cells by qRT-PCR. Scale bar: 100 μm. $^{*}P < 0.05$, $^{**}P < 0.01$, $^{***}P < 0.001$, $^{****}P < 0.0001$ *vs.* normal group; $^{\#}P < 0.05$, $^{\#\#}P < 0.01$, $^{\#\#\#}P < 0.001$, $^{\#\#\#\#}P < 0.0001$. Data are presented as mean ± SD ($n \geq 3$).

(H&E) staining. As shown in Fig. 3E, the lung tissue was in normal structure without infiltration of inflammatory cells for sham group. For ALI group, it was obviously observed that the lung was in the disordered state with thicken alveolar wall, and a huge amount of infiltrated inflammatory cells. However, P@Co + NIR obviously lowered the infiltrated cells with a thin alveolar wall. After scoring, it was 0.4 ± 0.2, 11.9 ± 0.8, 8.9 ± 0.4 and 4.4 ± 1.5 respectively for sham group, ALI group, P@Co and P@Co + NIR (Fig. 3F). Meanwhile, for immunohistochemical staining, IL-1β and TNF-α expression levels obviously increased for ALI group compared to sham group (Fig. 3G). P@Co could decrease the expression levels of IL-1β and TNF-α, where they were enhanced for P@Co + NIR (Fig. 3H). Furthermore, the HSP70 expression levels of lung tissue were also evaluated by immunohistochemical staining. As imaged in Fig. S26 (Supporting information), the obvious HSP70 expression was observed for P@Co + NIR, compared to other groups. Statistically, it was 0.9 ± 0.1, 0.3 ± 0.1, 1.0 ± 0.1 and 8.3 ± 0.5 for sham group, ALI group, P@Co and P@Co + NIR (Fig. S27 in Supporting information). At last, the other organs, like heart, liver, spleen and kidney were additionally evaluated by H&E staining. No damages were observed

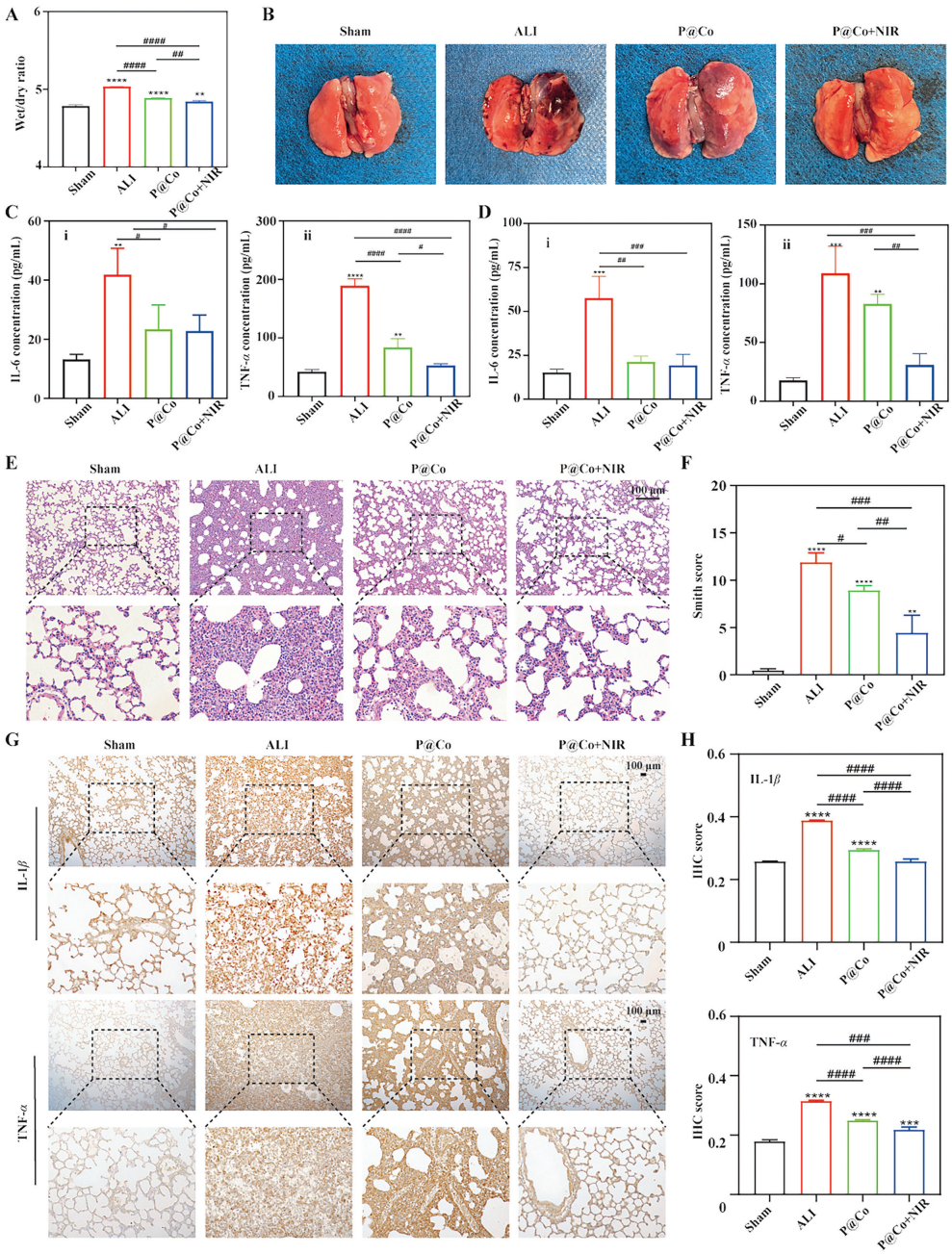

Fig. 3. *In vivo* therapy evaluation. (A) The wet/dry ratio of lung tissue of treated rats. (B) Macroscopic observation of lung tissue of treated rats. (C) Inflammatory factors (IL-6 (i) and TNF-α (ii)) expression levels of blood serum of treated rats by ELISA. (D) Inflammatory factors (IL-6 (i) and TNF-α (ii)) expression levels of lung homogenate of treated rats by ELISA. (E) H&E staining images of lung tissue of treated rats and the corresponding Smith score (F). (G) Inflammatory factors (IL-1β and TNF-α) expression levels of lung tissue of treated rats by immunohistochemical staining and the corresponding IHC score (H). Scale bar: 100 μm. $^{*}P < 0.05$, $^{**}P < 0.01$, $^{***}P < 0.001$, $^{****}P < 0.0001$ *vs.* normal group; $^{\#}P < 0.05$, $^{\#\#}P < 0.01$, $^{\#\#\#}P < 0.001$, $^{\#\#\#\#}P < 0.0001$. Data are presented as mean ± SD ($n \geq 3$).

in all other organs for ALI group, P@Co and P@Co + NIR respectively, consistent with sham group (Fig. S28 in Supporting information).

In this study, we successfully designed a novel strategy of nanozyme (P@Co) combining with NIR irradiation for synergistic treatment of ALI. P@Co was prepared by loading PDA with ultrasmall nanosized Co, achieving enhanced ROS scavenging. The excellent antioxidant and anti-inflammatory capacities were demonstrated *in vitro* and *in vivo* through the down-regulation of inflammatory factors and intracellular ROS levels, as well as induction of M2 directional polarization. Significantly, it presented outstanding biocompatibility and biodegradability, indicated by accumulation in the lung and gradually degradation. In conclusion, it offered a promising strategy in clinical treatment of ALI and other ROS derived diseases.

Declaration of competing interest

The authors declare that they have no known competing financial interests or personal relationships that could have appeared to influence the work reported in this paper.

CRediT authorship contribution statement

Xiaoshuai Wu: Writing – original draft, Conceptualization. **Bailei Wang:** Formal analysis. **Yichen Li:** Methodology. **Xiaoxuan**

Guan: Data curation. **Mingjing Yin:** Software. **Wenquan Lv:** Visualization. **Yin Chen:** Validation. **Fei Lu:** Investigation. **Tao Qin:** Project administration. **Huyang Gao:** Investigation. **Weiqian Jin:** Investigation. **Yifu Huang:** Formal analysis. **Cuiping Li:** Resources, Project administration, Funding acquisition. **Ming Gao:** Writing – review & editing, Supervision, Resources, Project administration, Methodology. **Junyu Lu:** Writing – review & editing, Supervision, Resources, Project administration.

Acknowledgments

This study was financially supported by the Key Research & Development Program of Guangxi (No. GuiKeAB22080088), the Joint Project on Regional High-Incidence Diseases Research of Guangxi Natural Science Foundation (No. 2023GXNSFDA026023), the Natural Science Foundation of Guangxi (No. 2023JJA140322), the National Natural Science Foundation of China (No. 82360372), the High-level Medical Expert Training Program of Guangxi "139" Plan Funding (No. G202003010), and the Medical Appropriate Technology Development and Popularization and Application Project of Guangxi (No. S2020099).

Supplementary materials

Supplementary material associated with this article can be found, in the online version, at doi:10.1016/j.cclet.2024.110211.

References

[1] J. Yao, X. Chen, F. Meng, et al., Brain Behav. Immun. 115 (2024) 109–117.
[2] I. Martin-Loeches, L.F. Reyes, S. Nseir, et al., Intensive Care Med. 49 (2023) 1212–1222.
[3] N.J. Meyer, L. Gattinoni, C.S. Calfee, Lancet 398 (2021) 622–637.
[4] L.D.J. Bos, L.B. Ware, Lancet 400 (2022) 1145–1156.
[5] H. Li, X. Chen, J. Xu, et al., Hepatology 79 (2024) 392–408.
[6] R. Yuan, Y. Li, S. Han, et al., ACS Cent. Sci. 8 (2022) 10–21.
[7] Y. Zhao, Z. Zhang, Z. Pan, et al., Exploration 1 (2021) 20210089.
[8] H. Li, P. Yang, J. Hwang, et al., Biomater. Transl. 3 (2022) 162–171.
[9] M. Chang, Z. Wang, C. Dong, et al., Adv. Mater. 35 (2023) e2208817.
[10] Y. Li, J. Lin, Y. He, et al., Exploration 3 (2023) 20230054.
[11] X. Li, L. Chen, M. Huang, et al., Asian J. Pharm. Sci. 18 (2023) 100775.
[12] M. Wang, P. Ma, J. Lin, Chin. Chem. Lett. 34 (2023) 108300.
[13] D. Furtado, M. Björnmalm, S. Ayton, et al., Adv. Mater. 30 (2018) e1801362.
[14] Z. Geng, Z. Cao, J. Liu, Exploration 3 (2023) 20210117.
[15] D. Li, E. Ha, Z. Zhou, et al., Adv. Mater. 1 (2023) e2308747.
[16] M.L. Alfieri, T. Weil, D.Y.W. Ng, et al., Adv. Colloid. Interface Sci. 305 (2022) 102689.
[17] B. Chen, L. Mei, R. Fan, et al., Asian J. Pharm. Sci. 18 (2023) 100781.
[18] N. Chen, W. Fu, J. Zhou, et al., Chin. Chem. Lett. 32 (2021) 2405–2410.
[19] H. Hu, X. Liu, J. Hong, et al., J. Colloid. Interface Sci. 612 (2022) 246–260.
[20] Y. Li, L. Yang, Y. Hou, et al., Bioact. Mater. 18 (2022) 213–227.
[21] S. Shahrokhian, S. Rezaee, Electrochim. Acta 259 (2018) 36–47.
[22] Y. Chen, H. Zou, B. Yan, et al., Adv. Sci. 9 (2022) e2103977.
[23] A. Jin, Y. Wang, K. Lin, et al., Bioact. Mater. 5 (2020) 522–541.
[24] P. Chen, Z. Li, D. Zhang, et al., Chin. Chem. Lett. 34 (2023) 108346.
[25] P.B. Balakrishnan, N. Silvestri, T. Fernandez-Cabada, et al., Adv. Mater. 32 (2020) e2003712.
[26] F. Cao, L. Zhang, Y. You, et al., Angew. Chem. Int. Ed. 59 (2020) 5108–5115.
[27] S. Cai, J. Liu, J. Ding, et al., Angew. Chem. Int. Ed. 61 (2022) 61-48.
[28] W. Liu, X. Song, W. Liu, et al., Chem. Mater. 34 (2022) 10606–10622.
[29] Y. Xing, L. Li, Y. Chen, et al., ACS Nano 17 (2023) 6731–6744.
[30] H. Zhu, S. Huang, M. Ding, et al., ACS Appl. Mater. Interfaces 14 (2022) 25183–25196.
[31] M. Bao, K. Wang, J. Li, et al., Acta Biomater. 161 (2023) 250–264.
[32] Z. Li, Y. Feng, S. Zhang, et al., ACS Nano 17 (2023) 8551–8563.
[33] X. Chen, Y. Yang, Q. Mai, et al., Biomaterials 304 (2024) 122384.